PNAS

Effect of skull morphology on fox snow diving

Jisoo Yuk[a], Anupam Pandey[a,b], Leena Park[a,c] (iD), William E. Bemis[d] (iD), and Sunghwan Jung[a,1] (iD)

Certain fox species plunge-dive into snow to catch prey (e.g., rodents), a hunting mechanism called mousing. Red and arctic foxes can dive into snow at speeds ranging between 2 and 4 m/s. Such mousing behavior is facilitated by a slim, narrow facial structure. Here, we investigate how foxes dive into snow efficiently by studying the role of skull morphology on impact forces it experiences. In this study, we reproduce the mousing behavior in the lab using three-dimensional (3D) printed fox skulls dropped into fresh snow to quantify the dynamic force of impact. Impact force into snow is modeled using hydrodynamic added mass during the initial impact phase. This approach is based on two key facts: the added mass effect in granular media at high Reynolds numbers and the characteristics of snow as a granular medium. Our results show that the curvature of the snout plays a critical role in determining the impact force, with an inverse relationship. A sharper skull leads to a lower average impact force, which allows foxes to dive head-first into the snow with minimal tissue damage.

impact dynamics | biomechanics | fox | snow | skull

Many animal species interact with the air–water interface (1, 2). Examples include gannets diving into water to catch their food (3), humans cliff diving for sport (4, 5), basilisks walking on the water surface (6), and dolphins porpoising (7). Accordingly, there have been studies about the mechanical properties and impact force of this air–water interface (8–11). On the other hand, interaction with snow is mostly limited to the winter sports of ski jumping and freestyle skiing, where low friction of compacted snow is exploited to slide at high speeds. Thus, mechanics of animals or people penetrating the air-snow interface is less known.

In nature, red foxes (*Vulpes vulpes*) and arctic foxes (*Vulpes lagopus*) dive into snow to catch prey, a behavior known as "mousing." These foxes can identify the location of animals under several feet of snow through their exceptional sensitivity to rustling noises (12), which have the peak in 2 to 10 kHz frequencies (13, 14). When foxes detect prey location and swiftly leap into snow at speeds of 2 to 4 m/s, they catch their prey completely by surprise.

Previous studies explored this mousing behavior in terms of the diving mechanism and success rate (15). Red foxes tend to jump in a north-easterly direction, and the success rate of hunts was much higher when the foxes jumped in this direction, in comparison to all other directions, suggesting that foxes use the Earth's magnetic field to hunt. However, the mechanical aspects of snow diving, which are also critical to hunting success, are not well understood.

An understanding of snow properties is needed to understand the mechanisms of snow diving. Snow is generally considered a granular medium, and many studies have shown its granular characteristics through experiments and simulations (16, 17). Interestingly, when objects are dropped onto a granular medium, the impact force shows a fluid-like behavior of the medium at high Reynolds numbers (18, 19). The impact force on a granular medium can be characterized by a change in the added mass (20), which is commonly used in objects impacting in fluids. Given the high speed of fox diving, we assume that the snow behaves as a fluid at high Reynolds number regime. Based on this, we develop a model using hydrodynamic added mass to estimate the impact force on fox skulls penetrating snow. In this study, we investigate how the head shape of foxes may relate to their ability to dive into snow at the initial phase. This is crucial because foxes dive first with their snouts, which might be susceptible to injury because they lack anatomical specializations for shock absorption. Similarly, woodpeckers have evolved a distinctive hyoid bone structure that wraps around their brains (21, 22). By understanding the effect of skull shapes on impact force in early-phase snow diving, we can get insights into effectiveness and safety of the mousing strategy.

Significance

In our study, we examine the hunting technique employed by red and arctic foxes, known as "mousing," wherein they dive head-first into snow to capture prey. Our research highlights the significance of skull morphology, specifically the curvature of the snout, in mitigating the impact forces endured by foxes during snow diving. Our findings show that the initial impact phase of fox snow diving closely resembles the behavior of fluids at high Reynolds numbers. This insight sheds light on the biomechanics of these unique hunting behaviors, offering valuable contributions to our understanding of animal adaptations and their interactions with their environment.

[1]To whom correspondence may be addressed. Email: sunnyjsh@cornell.edu.

Results

Snow-Diving Fox. From several nature documentaries, we obtained video footage of successful mousing behavior by red foxes and arctic foxes (23–27). These videos revealed that foxes carefully sense the sounds of prey moving under the snow to pinpoint their prey. Once their prey is located, the foxes assume a stance, jump upward, and dive head first into the snow to capture their prey. To analyze the fox's kinematics, we used the video clips from online sources to extract their velocity profile and vertical position.

When a fox dives into snow, the head lands almost vertically on the snow surface and the tip of the snout touches the snow first (Fig. 1A). The fox can further penetrate the snow using the forelimbs to push the head and upper body below the snow surface, depending on the depth of their prey. To study the early dynamics of impact and head penetration, we tracked the tip of the snout to calculate its velocity profile and vertical position (Fig. 1B). The maximum height reached during a jump is approximately 50 to 60 cm above the snow and the maximum speed at which the fox impacts the snow surface can be as high as 4 m/s. Using the average dive height and speed obtained from video analyses, we reproduced the diving behavior of the fox in our lab.

Comparative Analysis between Canidae and Felidae. We selectively explored phylogenetic relationships of species within the carnivore families Felidae and Canidae to investigate morphological features related to mousing (Fig. 2A). Carnivora has 12 families including Felidae and Canidae, and most use sharp canine teeth to kill prey. However, other morphological features vary depending on the type and size of prey and habitat. For example, felids have a round and short snout with a wider muzzle (e.g., *Lynx* and *Puma*, Fig. 2). Having a short powerful jaw is typical of felids, which are specialized for solitary hunting. Because the canine teeth are located relatively closer to the jaw joint than they are in canids, a felid can make a strong killing bite (28). In addition, a wider muzzle of a felid enables it to bite larger prey.

Canids, which often hunt in groups, have relatively a longer snout than do felids (grayscale images in Fig. 2A). Within Canidae, there are slight differences between the genera *Vulpes* and *Lycalopex*. For instance, the palatine bones of *Lycalopex* extend posteriorly beyond the end of the tooth row whereas the palatine bones of foxes in the genus *Vulpes* do not (29). Fig. 2A shows skulls for 8 of the 12 species of *Vulpes* and for three of the subspecies of the red fox, *V. vulpes*. These taxa exhibit varying degrees of morphological adaptation in terms of size and tooth structure related to factors such as competition, diet, geography, and environment. Red foxes occur in all of these biomes (deserts, forests, grasslands, and tundra) and have the largest species range of any member of Carnivora, but the arctic foxes (*V. lagopus*) live exclusively in the cold tundra region. As an adaptation for cold climates, arctic foxes underwent positive selection of genes associated with fatty acid metabolism differently from red foxes (30). Despite these differences, both the red and arctic foxes share a narrow, elongated muzzle (Fig. 2A).

Principal Component Analysis to Understand the Sharpness of Fox Snouts. We used principal component analysis to quantify relationships between species and morphological characteristics of the skull (Fig. 2 *B* and *C*). We included 36 specimens, including an arctic fox model with an intentionally reduced snout length. We developed this reduced snout model to better understand the effect of the snout. The snout in the model is 25% of its original length, but it preserves the shapes of structures posterior to the snout.

The first two principal components, PC1 and PC2, explain 86.3% and 2.9% of the total variation, respectively. PC1 strongly reflects the length of the snout, with higher values indicating a longer snout. PC2 relates to the convexness of the posterior parts of the skull near landmarks 18 and 19, with more convex and rounded shapes corresponding to lower values of PC2. Fig. 2C shows the clear separation of felids (*Lynx* and *Puma*) from canids (*Vulpes* and *Lycalopex*). Felid PC1 scores ranging from −0.2 to −0.1, whereas the canids range from 0 to 0.1. PC2 values range from −0.3 to 0.3 in both families. Interestingly, the artificially flattened arctic fox model is situated near the felids in the PCA results. This demonstrates that the snout of the flattened arctic fox model has been decreased sufficiently to resemble that of a bobcat (*Lynx*). Meanwhile, *Lycalopex* overlaps with *Vulpes*. Although *Lycalopex* and *Vulpes* exhibit osteological differences in the palate, our study did not find any significant difference in the dorsal view of the skull, for both share the common feature of long muzzles. In summary, PC1 is a parameter that indicates how elongated the snout is. The pronounced difference in PC1 between the felids
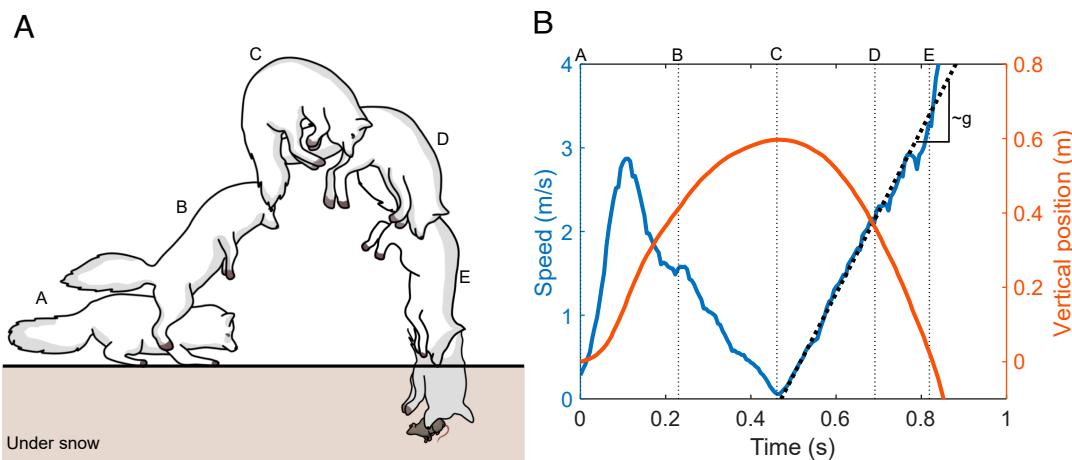
Fig. 1. (*A*) Schematic drawing of a fox snow diving, a behavior known as mousing. This schematic drawing is composed of scenes traced from the video of Creative #1150719032 (24). (*B*) Tracking data for the nose when an arctic fox dives into the snow. Data were obtained by analyzing the same video we traced in (*A*) (24). The left *y*-axis shows the speed, and the right *y*-axis shows the vertical position of the snout. Diving profiles for four other videos are provided in *SI Appendix*, Fig. S1.
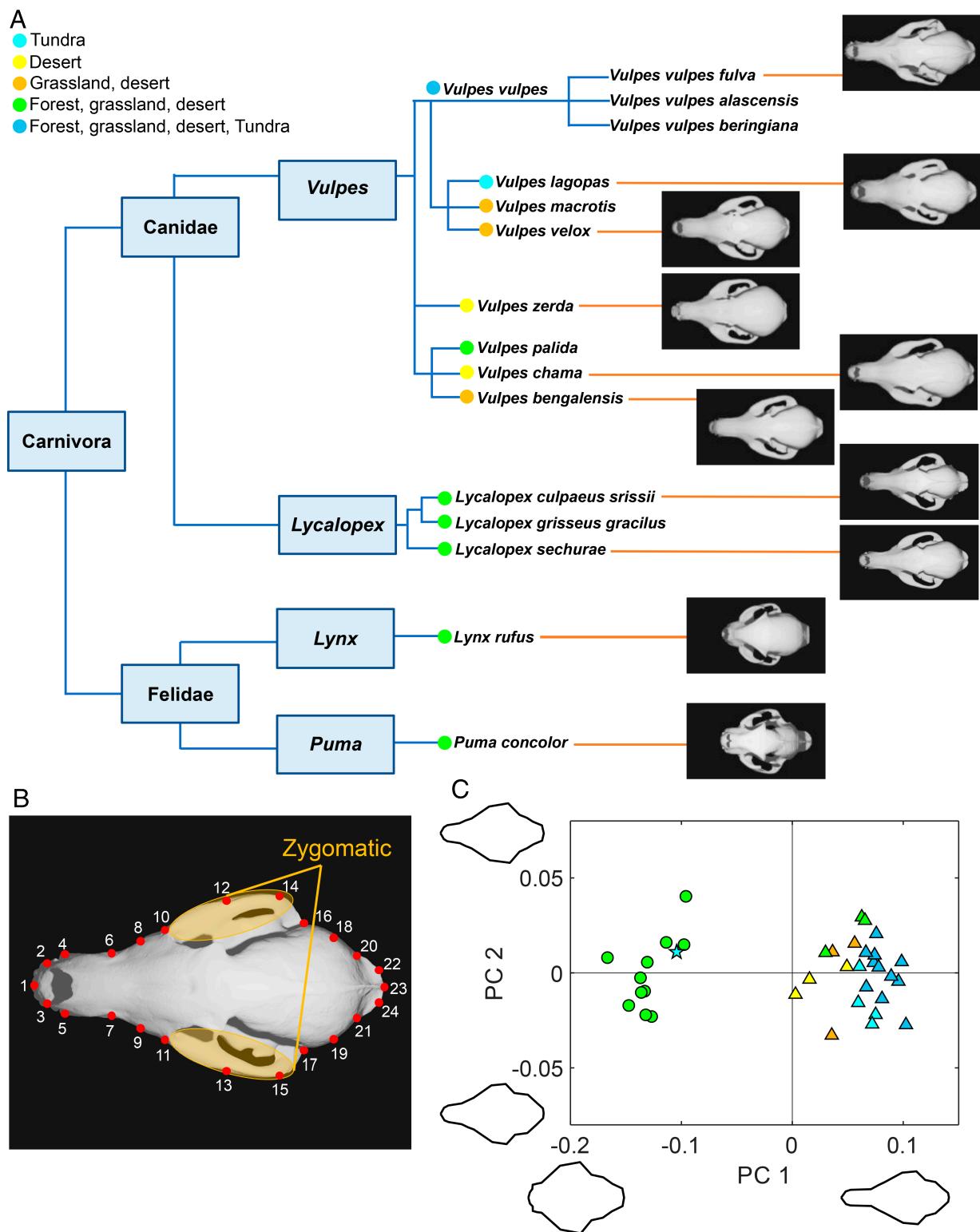
**Fig. 2.** (*A*) Phylogeny of Canidae and Felidae including *Vulpes*, *Lycalopex*, *Lynx*, and *Puma*. Color coding to the left of the species names indicates the habitat in which it occurs. Grayscale images to the right of the species name are dorsal view images of the skull. We scanned the grayscale skull images using specimens at the American Museum of Natural History (AMNH) in New York City and display the results as grayscale images. (*B*) Landmarks for PCA with arctic fox skull. The same landmarks were used for all species. (*C*) PCA results for the animals in the phylogenetic tree (*A*). The triangle and circle show Canidae and Felidae, respectively. The star symbol represents the reduced snout arctic fox model. PC1 represents the length of the skull, and PC2 plots how clearly the rear part of the zygomatic arch is distinguished.

and canids clearly suggests that foxes have notably sharper snouts compared to felids. We investigate whether this characteristic of foxes affects the impact force when passing through snow via physical experiments.

Physical Experiments into Water and Snow. To characterize how a narrow and elongated snout can penetrate snow during hunting, we conducted physical dropping experiments. We connected 3D printed fox skulls to a load cell and then directly
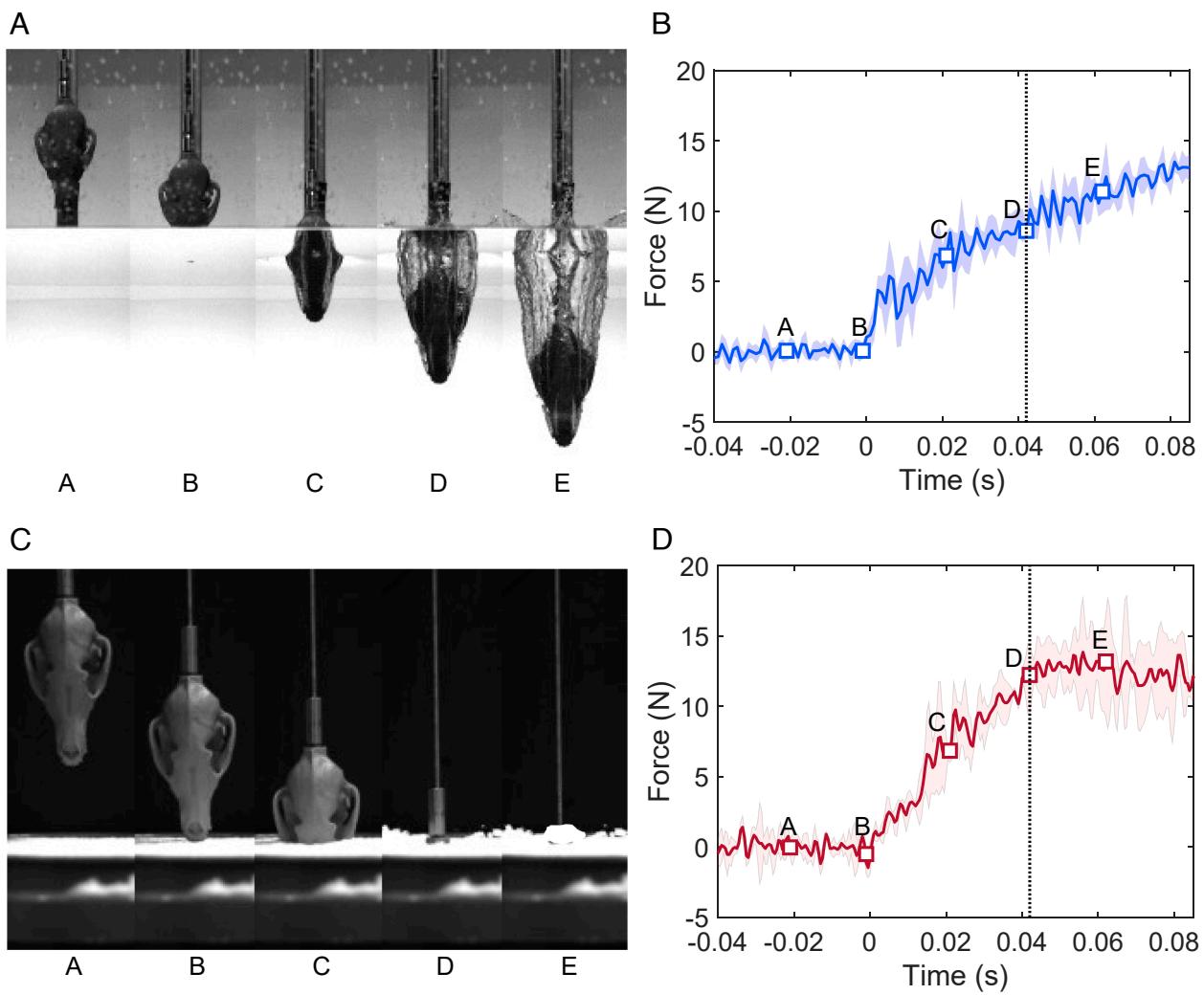
Fig. 3. (*A*) Image sequence of the arctic fox skull entering water. (*B*) Force versus time plot of the arctic fox diving into water. (*C*) Image sequence of the arctic fox skull entering snow. (*D*) Force versus time plot of the arctic fox diving into snow. The snow density of this experiment is 106 kg/m³.

dropped them into both water and snow. While water is not the natural medium for foxes to dive into, testing the skull in water offered two benefits. First, water is a well-characterized and stable medium. In contrast, snow is a granular material composed of a complex of ice crystals and flakes with unique properties of porosity and compressibility. These snow properties are influenced by environmental factors such as temperature, density, humidity, particle size, etc. (31–33). Experiments with water can be conducted year-round, but there are seasonal limitations for obtaining fresh snow. Second, trends in the impact force in snow can be predicted from experiments in water using hydrodynamic added mass (18–20). The fox diving into water is also theoretically sufficient to be hydrodynamically interpreted with a high Reynolds number, more than 20,000. With this approach, we were able to establish a model for impact forces on snow. During the winter season, we conducted experiments by dropping printed skulls on snow and compared the impact force observed in snow with that in water to confirm the properties of snow as a granular medium.

We measured the impact force on a 3D-printed skull impacting on either water (Fig. 3 *A* and *B*) or snow (Fig. 3 *C* and *D*). At time A, the skull is dropped and at time B, it touches the interface and begins to penetrate. At time C, half of the skull passes through, and at time D, the skull is completely submerged. At time E, the penetration depth is approximately 1.5 times of the skull.

To link the observed sequences to force data, we first evaluated qualitative observations. The dropped fox skull has a distinctive elongated and streamlined shape with a narrow muzzle and a wider zygomatic arch. Because of this, the impact area increases as the skull penetrates the medium. Therefore, the force increases in both water and snow after the initial touchdown. The zygomatic arch demarcates the maximum area that must pass through the medium. If the medium is water, the skull enters the cavity phase just before time D. During this phase, forces on the skull will continue to increase due to hydrostatic pressure of the water. In contrast, the force does not continue to increase after time D in the snow experiment. Unlike water, the snow is a compressible and permeable solid that cannot hold a hydrostatic force. Rather, the snow has a crater once compressed and does not return to its previous state. The presence or absence of hydrostatic pressure is a major difference between water and snow, but they show similar tendencies in the initial impact phase.

Impact Force on Fox Skulls. The impact force on the snow is estimated and compared to experimental data. The impact force during the impact phase is determined by media properties and relative velocity of the projectile. As snow dynamics upon impact are not well understood, we assume that the impact dynamics on snow are similar to those on water. Under this assumption, the impact force is calculated based on changes in added mass at a

constant velocity. Hydrodynamic impact force can be expressed as $F = V^2 dm_a/dz$, where V is the impact velocity, m_a is the added mass, and z is a downward-pointing direction. The added mass term is modified using von Karman's model (8) and geometries of animal bodies (3, 4). According to von Karman's model, added mass term can be represented by the instantaneous hemispherical liquid volume, $m_a = (2/3)\rho\pi r(t)^3$ (34, 35), where ρ is the fluid density and r is the radius of the hemisphere depending on the wetted area. This is further modified with geometrical approximation, $r = (z/\kappa_m)^{1/2}$ and $z = Vt$ where κ_m is the curvature of the object and t is time. The impact force finally becomes

$$F = \alpha\beta\rho V^{5/2}\kappa_m^{-3/2}t^{1/2}, \qquad [1]$$

where α is a prefactor determined by the shape of a projectile (in this case $\alpha = 2$ (4), which is obtained based on the results of water tests), β is a fitting parameter depending on the properties of the medium. In this expression, curvature is an important parameter that determines the force. Thus, it is essential to examine the overall shape of the fox skull more closely to measure the curvature accurately. To measure the precise curvature, the fox skull is divided into two parts—the front region of the snout and the rear region around the zygomatic arch (*SI Appendix,* Fig. S2). This classification is due to the abruptly widening width

at the zygomatic arch while remaining relatively consistent at the muzzle. For the approximation, we assume that the original snout is covered by a first spheroid with a higher curvature, κ_{m1}, and the zygomatic arch is approximated as a second spheroid with a lower curvature, κ_{m2}. The spheroid fit is performed using the least square method to fit the actual skull the best. The impact force over time is eventually estimated using the curvature at the lowest point along the z axis of each spheroid.

The fitting parameter β, is introduced to align with the experimental data. The force calculated by Eq. **1** is plotted in Fig. 4*C*. For snow, a value of $\beta = 11$ provides a good fit to the experimental data, whereas for water, $\beta = 1$. This variation in β values might be attributed to the differing properties of the two media. For example, snow has the unique feature of compressibility consisting of 1 to 10% ice and the rest air. As a projectile penetrates the snow, it gradually compresses and locally gets dense as snow clumps. This compression process may generate additional force that does not occur in water and requires an extra factor like β to account for it. The 2D-wedge experiment supports the compressibility of snow. The corresponding video (in Movie S3 and *SI Appendix,* Fig. S4) shows the propagation of compression in snow. When a wedge is dropped, the air in the snow is compressed, resulting in local compaction. At the same time, the pressure from the impact of the wedge spreads slowly through the snow medium. This observation suggests that when
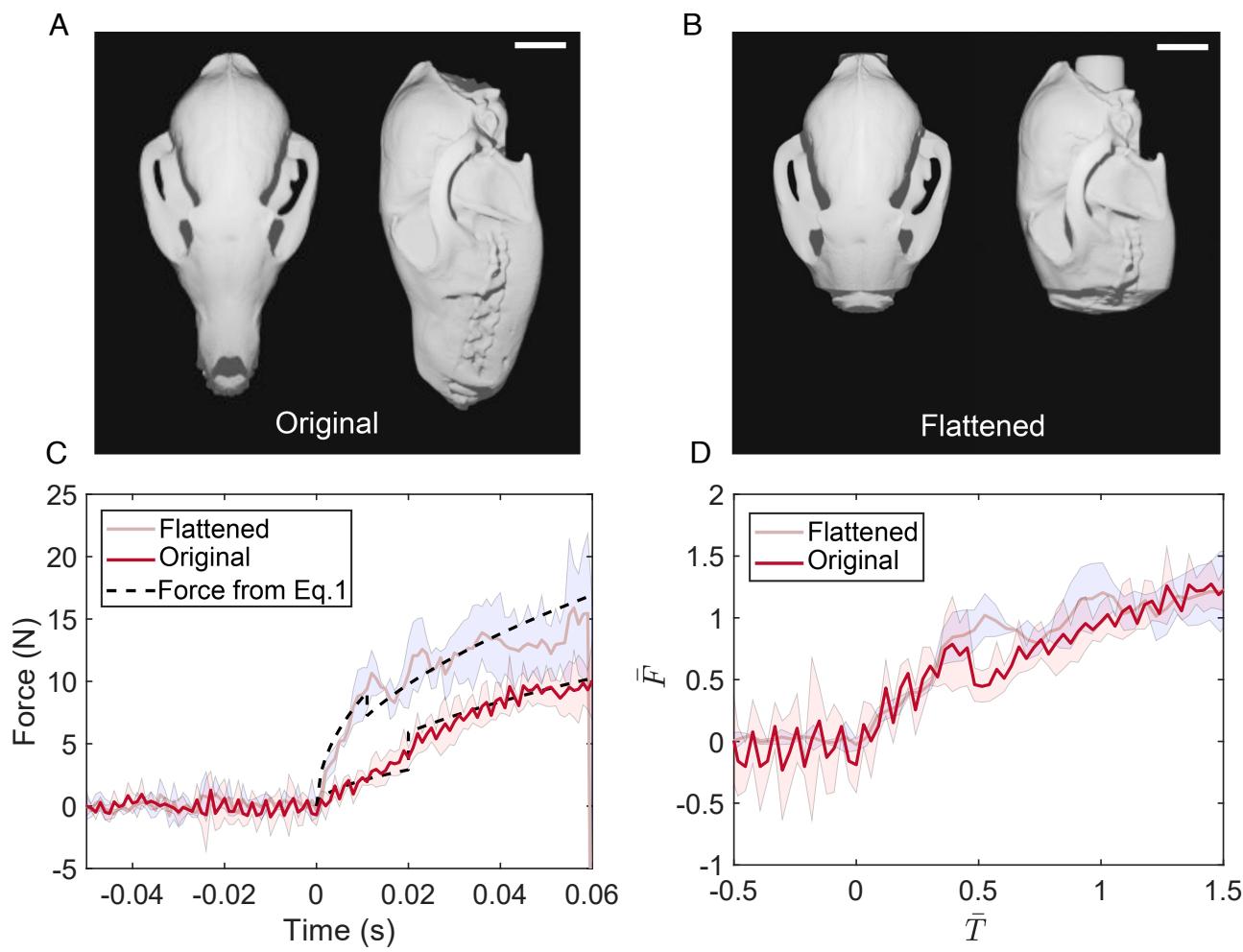

Fig. 4. (*A*) Dorsal view (*Left*) and side view (*Right*) of the original arctic fox skull. (Scale bar, 2 cm.) (*B*) Dorsal view (*Left*) and side view (*Right*) of the flattened snout arctic fox skull. The snout of the flattened model is reduced to 25% of its original length. (Scale bar, 2 cm.) (*C*) Force versus time when the flattened and original skulls dropped onto the snow. The black dash line shows the estimated force calculated using Eq. **1**. (*D*) Nondimensional force versus nondimensional time graph. In this experiment, the density of the snow is 87 kg/m³ for the original snout and 98 kg/m³ for the flattened snout.

a tapered object, such as a head of a fox, penetrates the snow, the pressure front may not propagate fast enough for prey to detect the pressure changes and escape. This could contribute to the advantage of foxes in mousing.

Next, a series of second experiments with a flattened snout model was conducted to evaluate the benefits of a longer snout length. Like the original model, we 3D printed the flattened model and connected to the force sensor, and dropped into snow. Results show that the flattened model generates a greater impact force in the initial phase compared to the original model, resulting in a substantial amount of total impact than the original model (Fig. 4C). This increase in force is due to the decrease in curvature in the flattened skull model as the snout length was reduced. We also computed the force from Eq. **1** in the same methodology as for the original snout model and found it is in good agreement with the experimental curves. This confirms that the Eq. **1** accurately describes the relationship between force and curvature.

Furthermore, experimental force of the original snout and flattened snout are normalized with the time and force when the skull is completely submerged. At the submerged time $t_s = H/V$, the impact force becomes $F_s = \alpha\beta\rho V^2 \kappa_m^{-3/2} H^{1/2}$, where the H is the length of the skull. Then, the nondimensional force becomes $\bar{F} = F/\alpha\beta\rho V^2 \kappa_m^{-3/2} H^{1/2}$, and the nondimensional time becomes $\bar{T} = tV/H$. The nondimensional force exhibited by both the original and flattened skulls follows a similar trend. However, when the nondimensional time is around 0.5, the nondimensional force on the original fox abruptly drops. This data trend represents the moment when the curvature changes from κ_{m1} to κ_{m2}. Since κ_{m2} is smaller than κ_{m1} in the original skull, the nondimensional force sharply decreases. On the other hand, for the flattened snout, the transition from κ_{m1} to κ_{m2} is relatively minor, resulting in a relatively smooth curve of nondimensional force.

To compare the overall magnitude of impact force of flattened and original snout, we quantified the time-averaged impulse. This physical quantity represents the average force applied to an object and the characteristics of the diving impulse and is defined as $I = \int_0^{t_s} F dt/t_s$. The calculation is shown in *SI Appendix*, Fig. S5. Results indicate that the diving impulse of the flattened snout is nearly double that of the original snout. This further supports the hypothesis that foxes with longer, high-curvature snouts are more efficient hunters as they generate a smaller impulse. Additionally, the longer snout would allow them to reach their prey deeper in the snow with less impact force.

Discussions

Our study allows us to understand the mechanisms of how foxes catch their prey by jumping into the snow with rapid leaps. First, we obtain the diving profile of red and arctic foxes from video tracking analysis. Next, we identify the morphological characteristics of the foxes' long snout through phylogenetic tree analysis and 3D scanning. Information about the habitat also helps us understand mousing behavior from an environmental perspective. Finally, we reproduce the snow diving behavior of foxes with 3D printed skulls and dropping tests. Through these physical tests, we can evaluate how the snout length can affect the impact force. The results reveal that the long and narrow snout allows foxes to penetrate the snow with less force compared to the flattened snout model.

Next, we observe snow's granular characteristics during impact. Snow's granular material properties have been studied to understand avalanche, but are not well studied for impact dynamics. Therefore, we were less certain that the snow would

behave like a granular material during impact dynamics. Our fox diving experiments demonstrate that the impact force trend during the early impact phase is similar in snow and water. This result strongly supports that snow behaves like a granular medium in impact dynamics. With this feature, the theoretical model for snow is constructed. This model shows the curvature of a snout is a key factor by negatively exponential to the impact force.

In summary, the elongated snout with higher curvature generates less impact force when it penetrates the snow, reducing the possibility of injury during impact. This skull shape also allows foxes to reach deeper into the snow, providing an advantage for catching small rodents located at greater depths. As a result, we predict that red and arctic foxes living in snow-covered areas will have a higher hunting success rate when mousing in snow.

However, there are limitations in our study. First, experiments were conducted using only the skull, not the entire body of the fox. As evident from the video analysis, the upper body part of foxes also submerged as well as the skull during mouse hunting. Therefore, the effect of the upper body on penetration was not assessed. In addition, we did not consider soft tissues (e.g., hair, skin, and muscles). Second, further research is needed on β. Here, β is a fitting parameter representing the compressibility property of the medium, which is independent of α but presumably depends on the density of the snow. However, our study could not investigate its dependency, since the snow density in our experiments ranges only from 87 to 106 kg/m³. This limited range was chosen to closely mimic the natural snow conditions encountered by foxes. Future experiments will be required to determine β at various densities and assess the relationship between β and density. Additionally, the variation in snow density at different depths, also needs to be considered as a factor affecting β. For example, as snow accumulates, the lower layers become more compacted due to weight, while the upper layers remain relatively fresh with lower density. Last, since penetration speed was held constant in our physical experiments, the influence of velocity would not be evaluated.

Nevertheless, our study is important because it shows that the morphology of the skull alone can explain the low impact force the fox experiences while snow diving. Furthermore, our research about the initial impact on snow is crucial for enhancing our understanding of how objects impact snow. This knowledge has practical implications for activities like ski jumping, skiing, and snowboarding, where falls often occur from elevated positions.

Materials and Methods

Skull Specimens. First, we visited the museums to gather 3D morphological information of mammal skulls. At the AMNH in New York City, a total of 13 different fox species skulls were scanned using the EinScan-SP (SHINING 3D, China) 3D scanner. The species and serial numbers of the specimens scanned are as follows: Arctic fox (*V. lagopus*, 18250), red fox (*V. vulpes*, 13906; 21814; 18244), swift fox (*Vulpes velox*, 14811), kit fox (*Vulpes macrotis*, 22696), fennec fox (*Vulpes zerda*, 90319), pale fox (*Vulpes pallida*, 82198), Cape fox (*Vulpes chama*, 81760), Bengal fox (*Vulpes bengalensis*, 54517), culpeo (*Lycalopex culpaeus*, 36454), South American gray fox (*Lycalopex griseus*, 41505), and Sechuran fox (*Lycalopex sechurae*, 46533). Meanwhile, at the Cornell Museum of Vertebrates, a total of 20 mammals including felids and canids were scanned using the PolyCam (2020) mobile app. The species and serial numbers of the specimens scanned are as follows: arctic fox (*V. lagopus*, 3913; 3914; 18047), red fox (*V. vulpes*, 8745; 8746; 8749; 10219; 10248; 10257; 10258; 10262), bobcat (*Lynx rufus*, 9178; 9490; 9615; 9660; 10057; 10128; 13958; 13989), and puma (*Puma concolor*, 13911).

To ensure that all sides of the skulls were scanned, we performed scans both in a forward and upside-down position. Then, the two scanned files were then merged into one using Blender software. We aligned them so that characteristic features such as tooth arrangement and zygomatic arch matched and then

merged them using the "join" function in Blender without further modification. The merged file was exported as stereolithography (STL) format. Additionally, we collected a few skulls' 3D information from CT-scan data. CT-scan images were obtained for the following species from Dr. Pamela Owen: Bobcat (*L. rufus*) (36). These CT-scan images were converted to a 3D STL file using the Slicer program. All the animal skulls were printed in full size using PLA filaments by an Ultimaker S5 printer (Ultimaker, Netherlands).

Landmarks and Principal Component Analysis. To quantify the morphological features of the skulls, we first captured dorsal view images from the 3D model of skulls. Along the outline of skulls, a total of 24 landmarks were selected. Using tpsUtil64 (Version 1.82) and tpsdig264 (Version 2.32) programs, landmarks were saved in thin-plate spline (TPS) format. The final analysis of the skulls' principal components was performed using the Geomorph package (Version 4.0.5) in R.

Video Analysis. From short footage of fox diving, we analyzed their speed and height profiles by Tracker software. To analyze the diving motion, the nose tip of the fox was selected as a point mass template, as it touches the snow very first during a vertical descent toward the ground. For the axis calibration, the average head to body length of the arctic fox and the tail length of the red fox were used as reference. The time calibration was based on the acceleration of the fox when the acceleration of the fox falling from its maximum height equaled the acceleration of gravity.

All the diving videos of foxes were sourced from the GettyImages website (www.gettyimages.com). All the videos we analyzed are listed below:

1. Slomo Arctic fox hunts on Tundra, Canada (Credit: BBC Natural History, Creative # 1150716601) (23)
2. Slomo Arctic fox hunts on Tundra, Canada (Credit: BBC Natural History, Creative # 1150719032) (24)
3. SLOMO Arctic fox hunts on Tundra, Canada (Credit: BBC Natural History, Creative # 1150681603) (25)
4. Red fox (*V. vulpes*) leaps into snow and catches rodent, Yellowstone, USA (Credit: BBC Natural History, Creative # 564830149) (26)
5. Red fox (*V. vulpes*) leaps into snow hunting rodents, Yellowstone, USA (Credit: BBC Natural History, Creative # 564829945) (27)

Water Test. Prior to the snow experiments, we conducted skull-drop experiments in water to understand how impact forces can be predicted. We built an experimental rig using 80/20 extrusion frames and installed it above a water tank. The original fox skull was positioned 50 cm above the water surface of the tank and then dropped. Force data were collected at a sampling rate of 1,000 Hz, and the motion of a skull was recorded at a speed of 4,000 frames per second with a high-speed camera. Force data and high-speed camera recordings were synchronized using a trigger. For more detailed information regarding the experimental setup and data synchronization, please refer to *SI Appendix*, section C.

Snow Test. To investigate the impact force of mousing behavior in foxes, drop experiments were conducted with 3D printed fox skulls connected to a load cell. In this experiment, we dropped the original arctic fox skull and the flattened arctic fox skull. These experiments were conducted exclusively during the cold winter months (January to March) when actual snow was available for testing (*SI Appendix*, section B and Table S1). The experiments took place at Riley-Robb Hall at Cornell University on a snowy day. For the test, we filled a 5-gallon bucket with uncompressed snow from the top layer of piled snow from outside and leveled the surface of the snow on the bucket. On the center of the bucket, we dropped each fox skull from a height of 50 cm. All the force data were collected at a sampling rate of 1,000 Hz and all motion was captured by a high-speed camera at 4,000 frames per second. The force data and high-speed camera images were synchronized through a trigger.

Pressure Propagation Test in Snow. For the pressure propagation experiment, we stacked fresh snow in a glass container and placed Black Diamond Premium Activated Carbon particles (Marineland, Blacksburg, VA) in the middle of the snow for visualization. Then, we dropped the 60-degree wedge onto the snow at a velocity of 3.6 m/s along the glass wall. All the dropping moments were recorded by a high-speed camera at a frame rate of 2,000 Hz. In this experiment, the density of snow with carbon particles was 160 kg/m^3, which is higher compared to other snow conditions due to the relative density of the carbon particles, which ranges from 1.8 to 2.1.

Data, Materials, and Software Availability. STL files for the original and flattened fox skulls, and the data and the Matlab code for the main figures have been deposited in OSF (https://osf.io/xfbsp/) (37).

1. J. Glasheen, T. McMahon, A hydrodynamic model of locomotion in the basilisk lizard. *Nature* **380**, 340–342 (1996).
2. S. T. Hsieh, G. V. Lauder, Running on water: Three-dimensional force generation by basilisk lizards. *Proc. Natl. Acad. Sci. U.S.A.* **101**, 16784–16788 (2004).
3. B. Chang *et al.*, How seabirds plunge-dive without injuries. *Proc. Natl. Acad. Sci. U.S.A.* **113**, 12006–12011 (2016).
4. A. Pandey, J. Yuk, B. Chang, F. E. Fish, S. Jung, Slamming dynamics of diving and its implications for diving-related injuries. *Sci. Adv.* **8**, eabo5888 (2022).
5. E. Gregorio, E. Balaras, M. C. Leftwich, Air cavity deformation by single jointed diver model entry bodies. *Exp. Fluids* **64**, 168 (2023).
6. J. W. M. Bush, D. Hu, Walking on water: Biolocomotion at the interface. *Annu. Rev, Fluid Mech.* **38**, 339–369 (2006).
7. B. Chang *et al.*, Jumping dynamics of aquatic animals. *J. R. Soc. Interface* **16**, 20190014 (2019).
8. T. Von Karman, The impact on seaplane floats during landing (Technical Notes No. 321, National Advisory Committee for Aeronautics, Washington, DC, 1929)
9. J. M. Aristoff, T. T. Truscott, A. H. Techet, J. W. Bush, The water entry of decelerating spheres. *Phys. Fluids* **22**, 032102 (2010).
10. T. T. Truscott, B. P. Epps, J. Belden, Water entry of projectiles. *Annu. Rev. Fluid Mech.* **46**, 355–378 (2014).
11. A. Kiyama, M. M. Mansoor, N. B. Speirs, Y. Tagawa, T. T. Truscott, Gelatine cavity dynamics of high-speed sphere impact. *J. Fluid Mech.* **880**, 707–722 (2019).
12. E. P. Malkemper, V. Topinka, H. Burda, A behavioral audiogram of the red fox (*Vulpes vulpes*). *Hearing Res.* **320**, 30–37 (2015).
13. G. Marimuthu, G. Neuweiler, The use of acoustical cues for prey detection by the Indian false vampire bat, *Megaderma lyra*. *J. Comp. Physiol. A* **160**, 509–515 (1987).
14. M. Konishi, How the owl tracks its prey: Experiments with trained barn owls reveal how their acute sense of hearing enables them to catch prey in the dark. *Am. Sci.* **61**, 414–424 (1973).
15. J. Červený, S. Begall, P. Koubek, P. Nováková, H. Burda, Directional preference may enhance hunting accuracy in foraging foxes. *Biol. Lett.* **7**, 355–357 (2011).
16. P. Bartelt, B. W. McArdell, Granulometric investigations of snow avalanches. *J. Glaciol.* **55**, 829–833 (2009).
17. P. Bartelt *et al.*, Modelling cohesion in snow avalanche flow. *J. Glaciol.* **61**, 837–850 (2015).
18. H. Katsuragi, D. J. Durian, Drag force scaling for penetration into granular media. *Phys. Rev. E* **87**, 052208 (2013).
19. M. Hou, Z. Peng, R. Liu, K. Lu, C. Chan, Dynamics of a projectile penetrating in granular systems. *Phys. Rev. E* **72**, 062301 (2005).
20. J. Aguilar, D. I. Goldman, Robophysical study of jumping dynamics on granular media. *Nat. Phys.* **12**, 278–283 (2016).
21. J. Y. Jung *et al.*, Structural analysis of the tongue and hyoid apparatus in a woodpecker. *Acta Biomater.* **37**, 1–13 (2016).
22. N. Lee *et al.*, The geometric effects of a woodpecker's hyoid apparatus for stress wave mitigation. *Bioinsp. Biomimet.* **11**, 066004 (2016).
23. BBC Natural History, "Slomo arctic fox hunts on Snowy Tundra, Canada." https://www.gettyimages.com/detail/video/slomo-arctic-fox-hunts-on-tundra-canada-stock-video-footage/1150716601. Accessed 8 December 2023.
24. BBC Natural History, "Slomo arctic fox hunts on Snowy Tundra, Canada." https://www.gettyimages.com/detail/video/slomo-arctic-fox-hunts-on-tundra-canada-stock-video-footage/1150719032. Accessed 8 December 2023.
25. BBC Natural History, "Slomo arctic fox hunts on Snowy Tundra, Canada." https://www.gettyimages.com/detail/video/arctic-fox-hunts-on-tundra-canada-stock-video-footage/1150681603. Accessed 8 December 2023.
26. BBC Natural History, "Red fox (*Vulpes vulpes*) leaps into snow and catches rodent, Yellowstone, USA." https://www.gettyimages.com/detail/video/red-fox-leaps-into-snow-and-catches-rodent-stock-video-footage/564830149. Accessed 8 December 2023.
27. BBC Natural History, "Red fox (*Vulpes vulpes*) leaps into snow hunting rodents, Yellowstone, USA." https://www.gettyimages.com/detail/video/red-fox-leaps-into-snow-hunting-rodents-stock-video-footage/564829945. Accessed 8 December 2023.
28. A. C. Kitchener, B. Van Valkenburgh, N. Yamaguchi, D. Macdonald, A. Loveridge, "Felid form and function" in *Biology and Conservation of Wild Felids*, D. Macdonald, A. Loveridg, Eds. (Oxford University Press, Oxford, United Kingdom, 2010), pp. 83–106.
29. F. A. Perini, C. Russo, C. G. Schrago, The evolution of South American endemic canids: A history of rapid diversification and morphological parallelism. *J. Evol. Biol.* **23**, 311–322 (2010).

30. V. Kumar, V. E. Kutschera, M. A. Nilsson, A. Janke, Genetic signatures of adaptation revealed from transcriptome sequencing of arctic and red foxes. *BMC Genom.* **16**, 1–13 (2015).

31. M. Mellor, Engineering properties of snow. *J. Glaciol.* **19**, 15–66 (1977).

32. J. Petrovic, Review mechanical properties of ice and snow. *J. Mater. Sci.* **38**, 1–6 (2003).

33. L. Canale *et al.*, Nanorheology of interfacial water during ice gliding. *Phys. Rev. X* **9**, 041025 (2019).

34. S. Jung, Swimming, flying, and diving behaviors from a unified 2D potential model. *Sci. Rep.* **11**, 1–11 (2021).

35. K. T. Patton, Hydrodynamic mass of bodies in a fluid in DTIC Report- USL-TM-933-351-64 (US Navy Underwater Sound Laboratory, Connecticut, 1964).

36. P. Owen, *Lynx rufus* (bobcat)–male–digimorph. Digimorph. https://www.digimorph.org/specimens/Lynx_rufus/male/. Accessed 8 December 2023.

37. S. Jung, Data from "Fox diving". OSF. https://osf.io/xfbsp/. Deposited 23 March 2024.